We are IntechOpen,
the world's leading publisher of
Open Access books
Built by scientists, for scientists

6,900
Open access books available

185,000
International authors and editors

200M
Downloads

154
Countries delivered to

Our authors are among the

TOP 1%
most cited scientists

12.2%
Contributors from top 500 universities

WEB OF SCIENCE™

Selection of our books indexed in the Book Citation Index
in Web of Science™ Core Collection (BKCI)

Interested in publishing with us?
Contact book.department@intechopen.com

Numbers displayed above are based on latest data collected.
For more information visit www.intechopen.com

Electronic States and Piezoresistivity in Silicon Nanowires

Koichi Nakamura, Dzung Viet Dao, Yoshitada Isono,
Toshiyuki Toriyama, and Susumu Sugiyama
Ritsumeikan University
Japan

1. Introduction

Recent progress in integrated-circuit processes can reduce the typical dimensions of the piezoresistive sensor to the microscale level to realize a micro-electro-mechanical systems (MEMS) device. However, size reduction causes a drastic loss in sensitivity for MEMS piezoresistive inertial sensors. For example, the sensitivity reduction of a MEMS piezoresistive accelerometer approximately is proportional to $1/L^3$–$1/L^4$ scaling, and 1 mm square may be the size limit for commercial applications (Sasaki et al., 2007). Therefore, a novel nanoscale piezoresistor with higher piezoresistance than bulk counterparts is necessary to fabricate microscale piezoresistive sensors free from sensitivity loss due to size reduction.

Single-crystal silicon has been one of the most important materials for piezoresistive sensors in MEMS or nano-electro-mechanical systems (NEMS) technology, because silicon has high crystallinity and mechanical stability even at the microscale level. These characters in silicon give a great expectation that some nanoscale mechanical sensors will be easily developed by the miniaturization of single-crystal silicon as component materials. However, the miniaturization should cause a drastic change in the electronic behavior in silicon even if the mechanical stability is maintained. In particular, low-dimensional materials such as nanosheets or nanowires have a radically different electronic state, that controls electrical conductivity, and accordingly, the piezoresistance coefficients in a low-dimensional nanomaterial would also be markedly different from those in the same material at the microscale level, combined with the large effect of strain and stress over the nanoscale material.

Silicon nanowire (SiNW) has been studied experimentally and theoretically as a particularly attractive candidate material composing MEMS/NEMS devices. We have succeeded in fabricating a p-doped single-crystal $\langle 110 \rangle$-oriented SiNW by electron beam (EB) direct writing and reactive ion etching (RIE) with a 50×50 nm^2 cross-sectional area in separation by implanted oxygen (SIMOX) substrate and in measuring the piezoresistance coefficients (Toriyama & Sugiyama, 2003). The SiNW we fabricated has a longitudinal piezoresistance coefficient $(\pi_{l\langle 110 \rangle})^p$ of 38.7×10^{-11} Pa^{-1} at a surface concentration N_s of 9×10^{19} cm^{-3}, which is 54.8% larger than that of the p$^+$ diffused microscale piezoresistor obtained by Tufte and Stelzer, $\pi_l = 25 \times 10^{-11}$ Pa^{-1} (Tufte & Stelzer, 1963).

Figure 1 shows the latest SEM image of one SiNW fabricated by our group (Tung et al., 2009). The width dependence of $(\pi_{l\langle 110\rangle})^p$ is shown in Fig. 2. As the width of SiNW gets thinner, the value of $(\pi_{l\langle 110\rangle})^p$ increases clearly. This result proves that the miniaturization of SiNW piezoresistor is extremely effective to improve the piezoresistive-based sensing function.
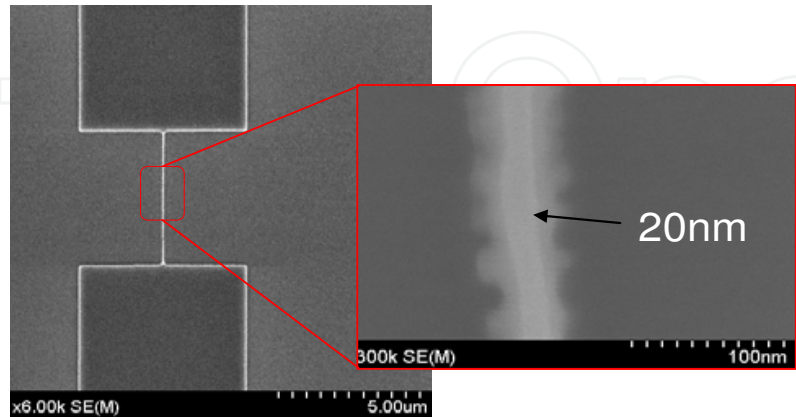

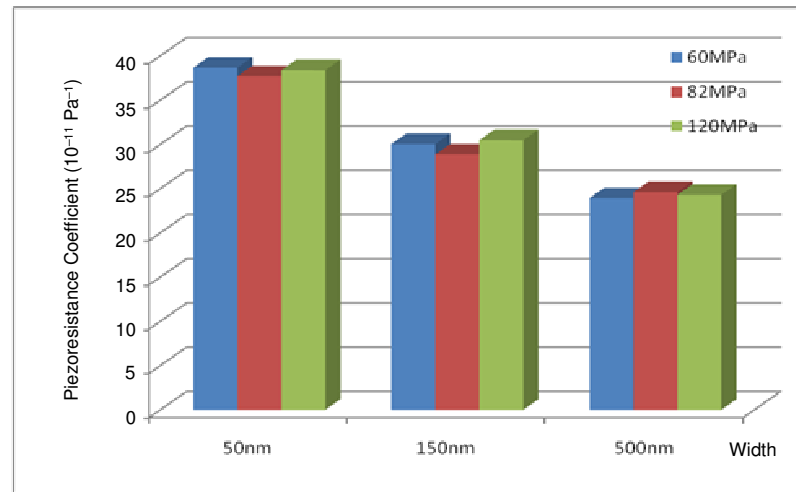Fig. 1. SEM image of 2-terminal p-SiNW piezoresistor: Longitudinal direction of SiNW is ⟨110⟩

Fig. 2. Longitudinal piezoresistance coefficient $(\pi_{l\langle 110\rangle})^p$ with respect to wire width of p-SiNW

Recently, He and Yang reported that p-doped ⟨111⟩ SiNW has a giant piezoresistance coefficient, $(\pi_{l\langle 111\rangle})^p = -3{,}550 \times 10^{-11}$ Pa^{-1}, according to their experimental measurement (He & Yang, 2006), and their experimental result of high piezoresistivity was supported through first-principles calculations of ⟨111⟩ SiNW without termination atoms at the wire wall (Cao et al., 2007), where the wave functions that contribute to hole transport were obviously localized in dangling bonds on the wire wall. However, dangling bonds are generally too reactive to exist for a long time; in general, they are attacked by oxygen, and occasionally by hydrogen (H) or halogen; therefore, piezoresistive properties of Si without dangling bonds will be practical in the application of MEMS/NEMS devices.

H-terminated SiNW models are effective for representing SiNW without dangling bonds. In this chapter, we present the simulation of the strain response to electronic states and the piezoresistance coefficients in H-terminated single-crystal SiNWs by using first-principles calculations of model structures with ⟨001⟩, ⟨110⟩, and ⟨111⟩ wire crystallographic-

orientations, in preparation for nanoscale piezoresistor applications (Nakamura et al., 2008; Nakamura et al., 2009a).

2. Method of calculation

2.1 First-principle calculation

We have carried out first-principles calculations of the periodic boundary models for bulk Si crystals and SiNW models using VASP (Kresse & Hafner, 1993; Kresse & Furthmüller, 1996) and FHI98md (Bockstedte et al., 1997) program packages, on the basis of the density functional theory (DFT) (Hohenberg & Kohn, 1964). For the DFT exchange-correlation interaction, the generalized-gradient approximation (GGA) method was used with the Perdew-Burke-Ernzerhof (PBE) functional (Perdew et al., 1996). We adopted the three-dimensional supercell approximation technique with norm-conserving pseudopotentials (Hamann, 1989). The cutoff energy for wave functions of electrons with plane-wave expansion was set at 40 Ry (544 eV) for bulk Si crystals and 30 Ry (408 eV) for SiNWs.

2.2 SiNW models

SiNW models have been devised by cutting out a fragment with a one-dimensional periodic boundary from the optimized bulk Si, and all dangling bonds of Si atoms were terminated with H atoms. The direction of the fragment with the one-dimensional periodic boundary can be defined as the longitudinal direction of SiNW, parallel to the z-axis in the three-dimensional supercell as shown in Fig. 3. We have devised ⟨001⟩, ⟨110⟩, and ⟨111⟩ SiNW models, according to the orientation of the fragment on the xy-plane, where the longitudinal direction is respectively set to [001], [110], and [111]. We have set up tetragonal supercells for ⟨001⟩ and ⟨110⟩ SiNW models, and a periodic boundary condition along the transverse directions, or perpendicular directions to the wire axis, was given by inserting sufficient space between H-terminated SiNWs with two large cell parameters of the supercell along x- and y-axes. For ⟨111⟩ SiNW models, hexagonal supercells have been introduced with two large cell parameters perpendicular to the z-axis.
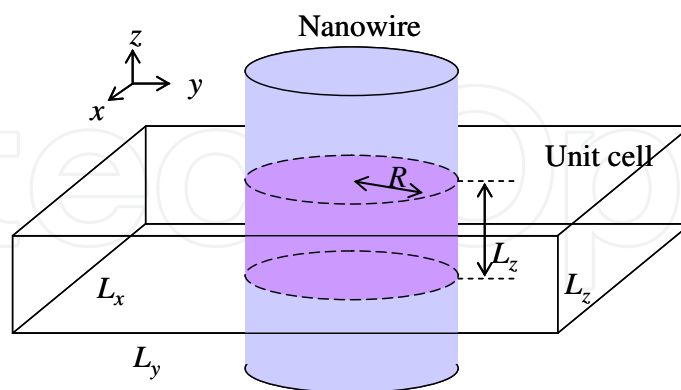

Fig. 3. Image of the tetragonal unit cell for SiNW periodic boundary model

The bulk Si crystal was regarded as a general diamond type, and we have optimized the cell parameters of a unit cell containing two Si atoms. We obtained the optimized cubic lattice constant of the diamond-type Si crystal as 5.463 Å. The effect of uniaxial tensile strain on structure was represented by partial optimization with a fixed lattice constant along the tensile direction. For 1% uniaxial tensile strain in the [001] direction, we set [001] lattice

constant at 5.518 Å and optimized [100] and [010] lattice constants to 5.449 Å, reduced by 0.25%. For 1% uniaxial tensile strain in the [110] direction, [001] lattice constants were optimized to 5.447 Å and [1$\bar{1}$0] translational vectors were slightly reduced by less than 0.01%. These fully and partially optimized parameters have been applied to structures of strain-free and tensile-strained SiNW models, respectively, as shown in Fig. 4.

Longitudinal stress

$L_z^* = L_z + \Delta L_z$
$R^* = R^*(\Delta L_z)$
(determined by Poisson ratio)

Transverse stress

$R^* = R + \Delta R$
$L_z^* = L_z^*(\Delta R); \; R'^* = R'^*(\Delta R)$
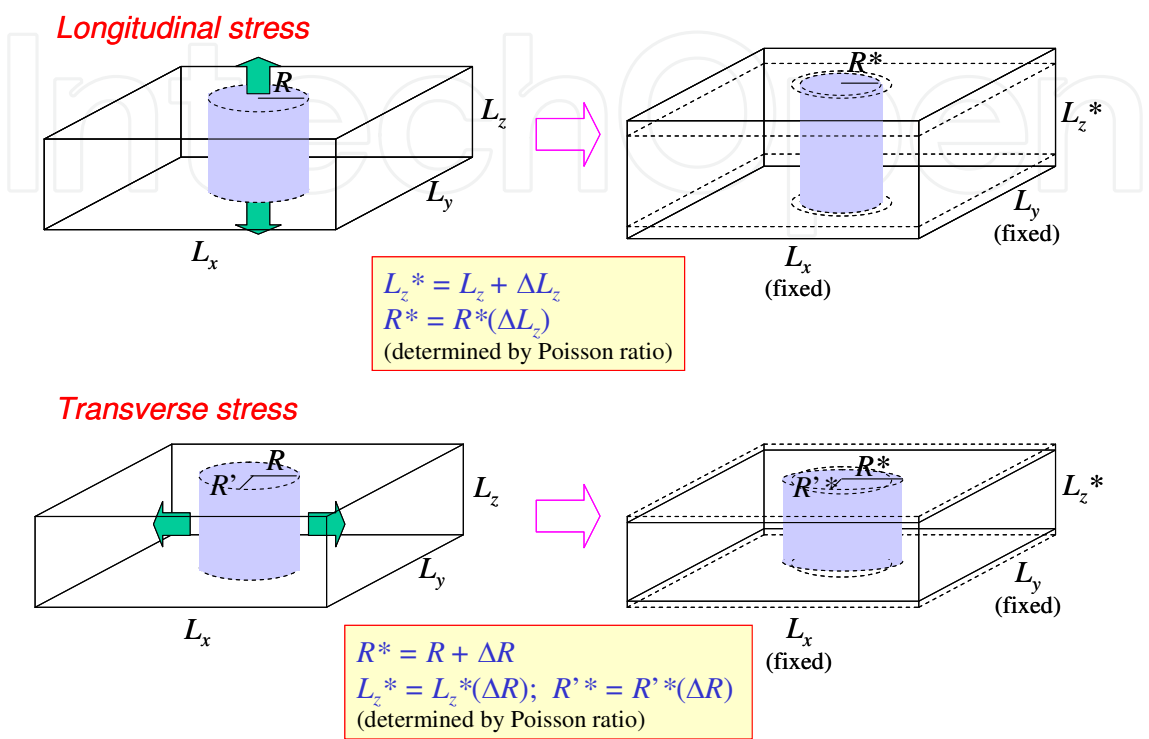(determined by Poisson ratio)

Fig. 4. Setting of tensile-strained SiNW models

Figure 5 displays the SiNW models we have devised in this chapter. Structural parameters of SiNW models and their unit cells are summarized in Table 1. The wire radius R is defined simply as the distance between the wire axis and the farthest nuclear including H atoms, and the volume of SiNW in the unit cell is determined by $V = \pi R^2 L_z$.

3. Band structures

The electronic band structure of each SiNW model was given in terms of the three-dimensional coordinates of the reciprocal space because we adopted the three-dimensional supercell approximation technique. An example of a band diagram for the three-dimensional band structure in the tetragonal Brillouin zone is shown in Fig. 6. Sufficient space between H-terminated SiNWs given by large cell parameters L_x and L_y causes band energies to be invariable along the transverse directions in the reciprocal space, for example, Z–R, X–Γ, Z–T, and M–Γ paths in the band diagram shown in Fig. 6. In other words, the invariance of band energies along these paths ensures "a piece of SiNW" without interaction between SiNWs. Thus, the band structure is reduced to be one dimensional, which is dependent on only one reciprocal coordinate, k_z, and therefore, the band diagram can only be represented along the Γ–Z path. For the hexagonal supercells, we have obtained the band structures that are dependent on only k_z with large transverse cell parameters as in the case of the tetragonal supercells. All of the band structures for strain-free SiNW models give a
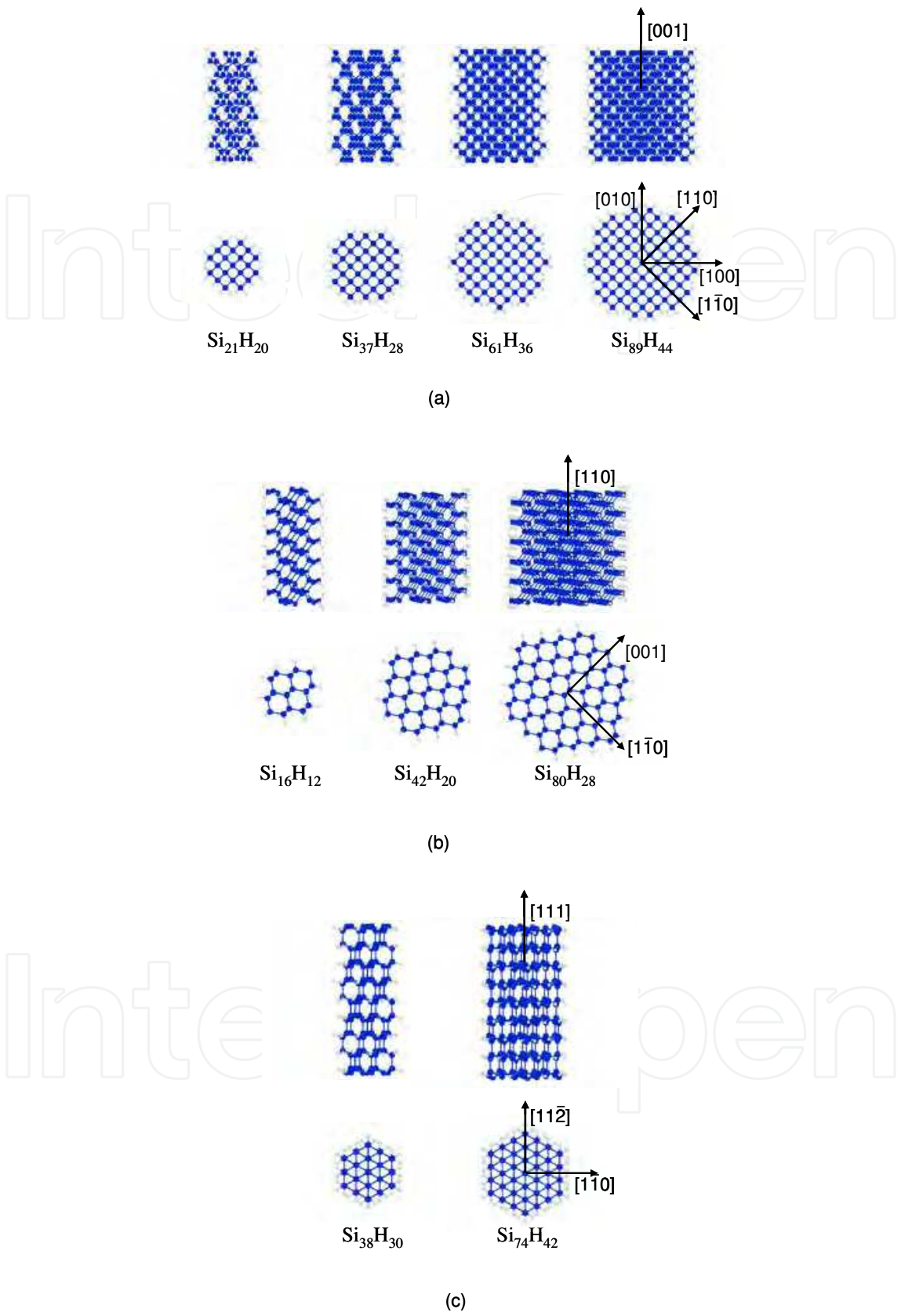
$Si_{21}H_{20}$ $Si_{37}H_{28}$ $Si_{61}H_{36}$ $Si_{89}H_{44}$

(a)

$Si_{16}H_{12}$ $Si_{42}H_{20}$ $Si_{80}H_{28}$

(b)

$Si_{38}H_{30}$ $Si_{74}H_{42}$

(c)

Fig. 5. Side and top views of H-terminated SiNW models: (a) ⟨001⟩ series with 4 unit cells, (b) ⟨110⟩ series with 6 unit cells, and (c) ⟨111⟩ series with 3 unit cells

	Radius	Cell parameters		
	R (Å)	L_x (Å)	L_y (Å)	L_z (Å)
$\langle 001 \rangle$ series				
$Si_{21}H_{20}$	5.435	13.229	13.229	5.463
$Si_{37}H_{28}$	7.272	16.934	16.934	5.463
$Si_{61}H_{36}$	9.149	21.167	21.167	5.463
$Si_{89}H_{44}$	11.044	25.401	25.401	5.463
$\langle 110 \rangle$ series				
$Si_{16}H_{12}$	5.641	13.229	13.229	3.863
$Si_{42}H_{20}$	9.075	21.167	21.167	3.863
$Si_{80}H_{28}$	12.899	27.517	27.517	3.863
$\langle 111 \rangle$ series				
$Si_{38}H_{30}$	5.865	13.229	13.229	9.463
$Si_{74}H_{42}$	8.096	18.521	18.521	9.463

Table 1. Structural parameters (referred to Fig. 3) of SiNW models and their tetragonal ($\langle 001 \rangle$ and $\langle 110 \rangle$ series) and hexagonal ($\langle 111 \rangle$ series) unit cells
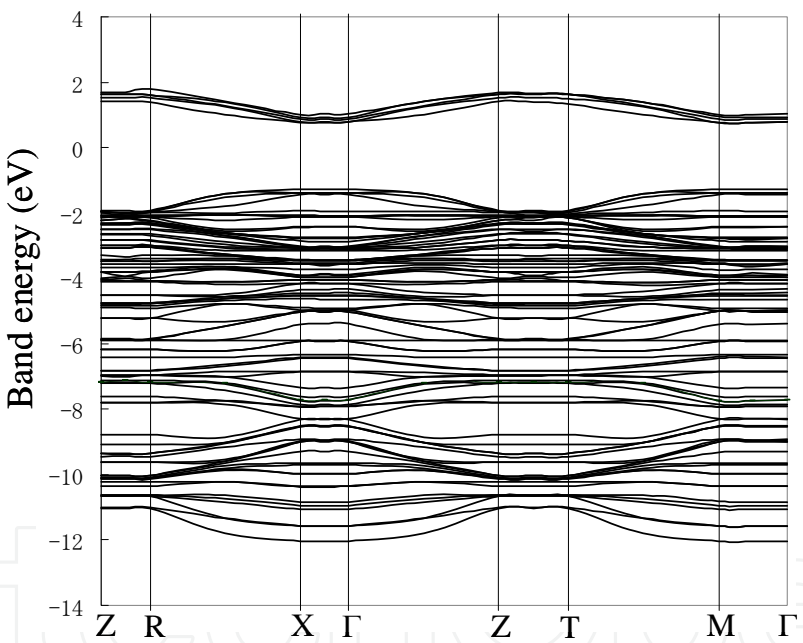

Fig. 6. Band energy diagram of $Si_{37}H_{28}\langle 001 \rangle$ SiNW model: R–X, Γ–Z, and T–M sections correspond to the longitudinal paths, and other sections are the transverse ones

direct band gap at the Γ point. As the radius of the SiNW model increases for each orientation series, the band gap gets lower and asymptotically approaches 0.612 eV, the computational value of band gap in bulk Si obtained by our calculation, as shown in Fig. 7. The transport properties of SiNWs have been discussed in terms of the band structures for $Si_{89}H_{44}\langle 001 \rangle$ (wire diameter $2R$ = 2.21 nm), $Si_{80}H_{28}\langle 110 \rangle$ ($2R$ = 2.58 nm), and $Si_{74}H_{42}\langle 111 \rangle$ ($2R$ = 1.62 nm) SiNW models, which respectively have the largest wire diameters in the $\langle 001 \rangle$, $\langle 110 \rangle$, and $\langle 111 \rangle$ series we have devised. The longitudinal tensile-strained model for $Si_{89}H_{44}\langle 001 \rangle$ SiNW has 1% strain in the [001] direction, and the transverse tensile-strained

model shows the same level in the [100] (or [010]) direction. The tensile-strained models for $Si_{80}H_{28}\langle 110 \rangle$ SiNW have 1% strain in the [110] direction as the longitudinal tension, or in the [$1\bar{1}0$] direction as the transverse tension. For $Si_{74}H_{42}\langle 111 \rangle$ SiNW, 1% strain is adopted in the [111] direction as the longitudinal tension, or in the [$1\bar{1}0$] direction as the transverse tension. We have observed the variations of the band structures with respect to strain on the SiNW models. Band diagrams in the vicinity of the valence-band (VB) top and the conduction-band (CB) bottom with/without tensile strain are shown in Figs. 8–13.
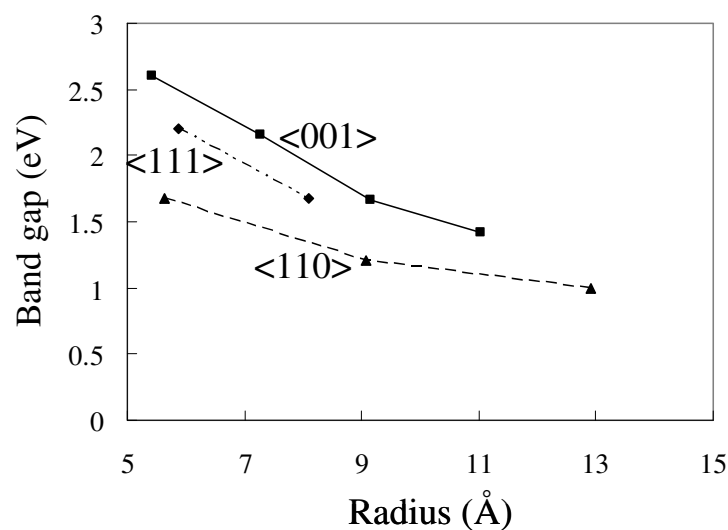

Fig. 7. Relationship between band gaps of SiNW models and wire radius

4. Theory of carrier conductivity

The electrical conductivity tensor G or the electrical resistivity tensor ρ can be represented in terms of carrier density and effective mass tensors (Kittel, 2005). Variations of band structure will exert an influence on them, and frequently contribute to a sudden turn of the conductivity. We have introduced the band carrier densities and their corresponding effective masses for each energy band, and the conductivity has been added up over all VB and CB subbands as follows,

$$G = \rho = e^2 \left(\sum_{j \in CB} n_j m_{e,j}{}^* \cdot \tau_{e,j} + \sum_{j \in VB} p_j m_{h,j}{}^* \cdot \tau_{h,j} \right), \qquad (1)$$

where n_j is the jth CB carrier electron density, p_j is the jth VB hole density, $m_{e,j}{}^*$ and $m_{h,j}{}^*$ are the effective mass tensors, $\tau_{e,j}$ and $\tau_{h,j}$ are the relaxation time tensors, and e^2 is the square of the absolute value of the elementary electric charge. Subscripts e and h respectively denote electron and hole carriers. The band carrier densities are controlled by the Fermi energy E_F and temperature T,

$$n_j = \frac{2}{V} \sum_{k_Z} w_{k_Z} \left\{ \exp\left(\frac{E_{j,k_Z} - E_F}{k_B T} \right) + 1 \right\}^{-1}; \qquad (2)$$
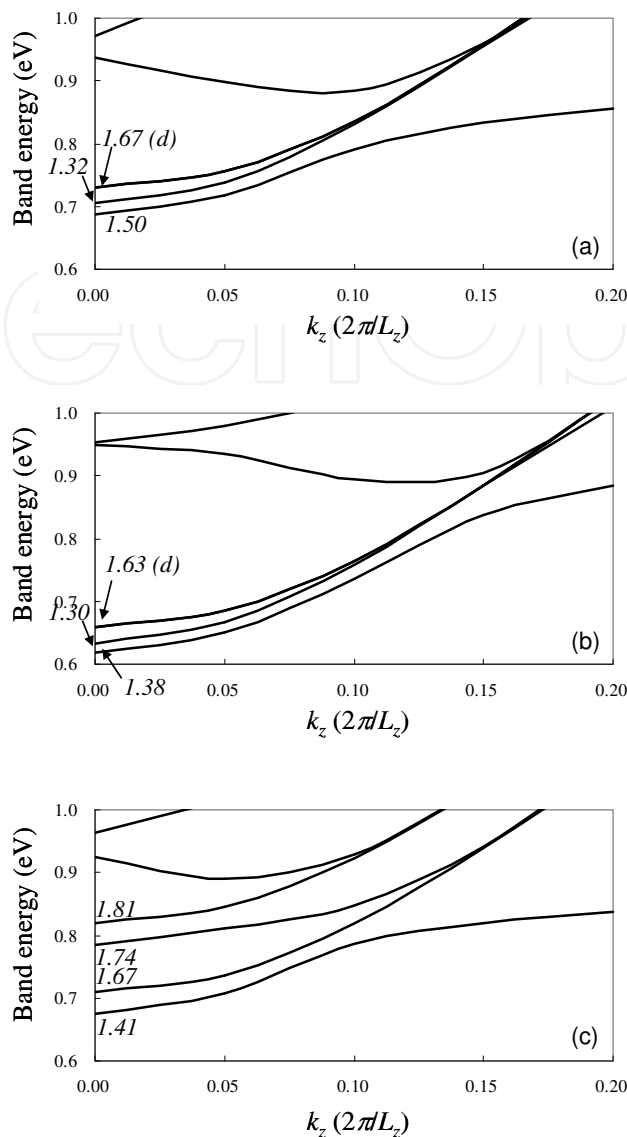
Fig. 8. Band diagram of $Si_{89}H_{44}\langle 001\rangle$ SiNW model in the vicinity of the conduction-band bottom (a) without stress, (b) with 1% longitudinal tensile stress, and (c) with 1% transverse tensile stress. Italic numbers denote the effective masses in units of m_0, the rest mass of an electron. *(d)* indicates degenerate subbands.

$$p_j = \frac{2}{V}\sum_{k_z} w_{k_z}\left\{\exp\left(-\frac{E_{j,k_z}-E_F}{k_B T}\right)+1\right\}^{-1}, \qquad (3)$$

where $E_{j,kz}$ is the band energy of the jth subband at the k_z point, w_{kz} is the k-point weight for k_z, V is the volume of SiNW in the unit cell, and k_B is the Boltzmann constant. We have performed a sampling with 11 k_z points along the Γ–Z path. In the intrinsic semiconductor state, these carrier densities should satisfy
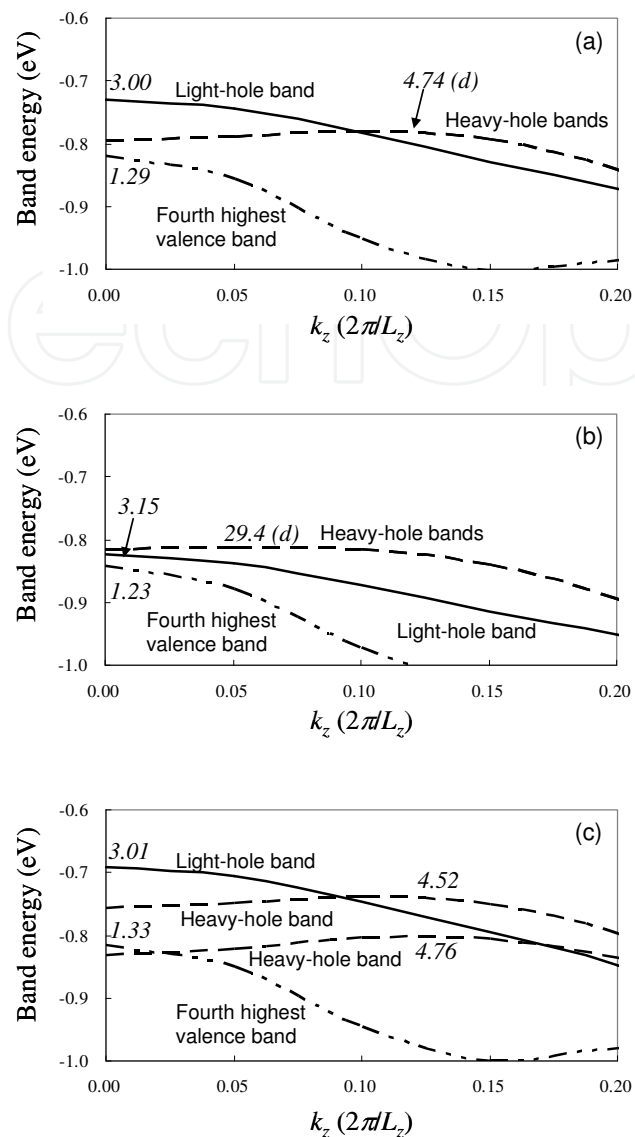
$$\sum_{j\in CB} n_j = \sum_{j\in VB} p_j . \qquad (4)$$

Fig. 9. Band diagram of $Si_{89}H_{44}\langle 001 \rangle$ SiNW model in the vicinity of the valence-band top: (a)–(c) denote the same conditions as those in Fig. 8. Italic numbers denote the effective masses in units of m_0. (d) indicates degenerate subbands.

Intrinsic semiconductors have only an infinitesimal number of carriers, so that n- or p-type semiconductors are generally applied to piezoresistive sensors. However, an excess or lack of electrons as large as one particle per unit cell in order to carry out regular first-principles calculation should lead to an enormous overestimation of carrier density, about 5×10^{20} cm^{-3}, for our SiNW models. In actual n- or p-type SiNWs, the total number of carriers per unit cell, δ, must be less by a few orders than 1. Under the condition that a small amount of the carrier occupation does not cause significant change in the band structure, δ can be given by an appropriate shift of the Fermi energy as

$$\delta = \sum_{j \in \mathrm{CB}} n_j' V = 2 \sum_{j \in \mathrm{CB}} \sum_{k_z} w_{k_z} \left\{ \exp\left(\frac{E_{j,k_z} - E_{\mathrm{F}}'}{k_{\mathrm{B}} T} \right) + 1 \right\}^{-1} \tag{5}$$
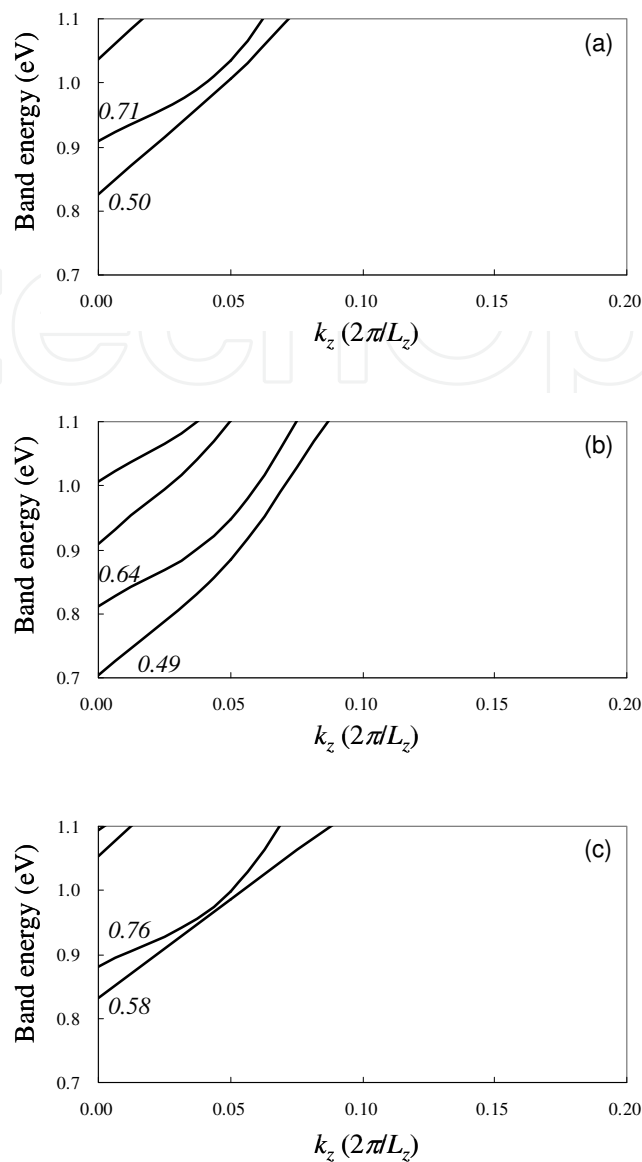
Fig. 10. Band diagram of $Si_{80}H_{28}\langle 110 \rangle$ SiNW model in the vicinity of the conduction-band bottom: (a)–(c) denote the same conditions as those in Fig. 8. Italic numbers denote the effective masses in units of m_0.

in the n-type carrier occupation with an upward shift of the Fermi energy updated to E'_F, or

$$\delta = \sum_{j \in VB} p'_j V = 2 \sum_{j \in VB} \sum_{k_z} w_{k_z} \left\{ \exp\left(-\frac{E_{j,k_z} - E'_F}{k_B T} \right) + 1 \right\}^{-1} \tag{6}$$

in the p-type carrier occupation with a downward shift, where the set of $\{E_{j,kz}\}$ is identical to that in the intrinsic semiconductor state. Practically, we first have set δ to an appropriate constant such as 10^{-n} ($n = 2, 3,$ and 4), and then E'_F in n- and p-type carrier occupations have been solved according to eqs. (5) and (6), respectively.

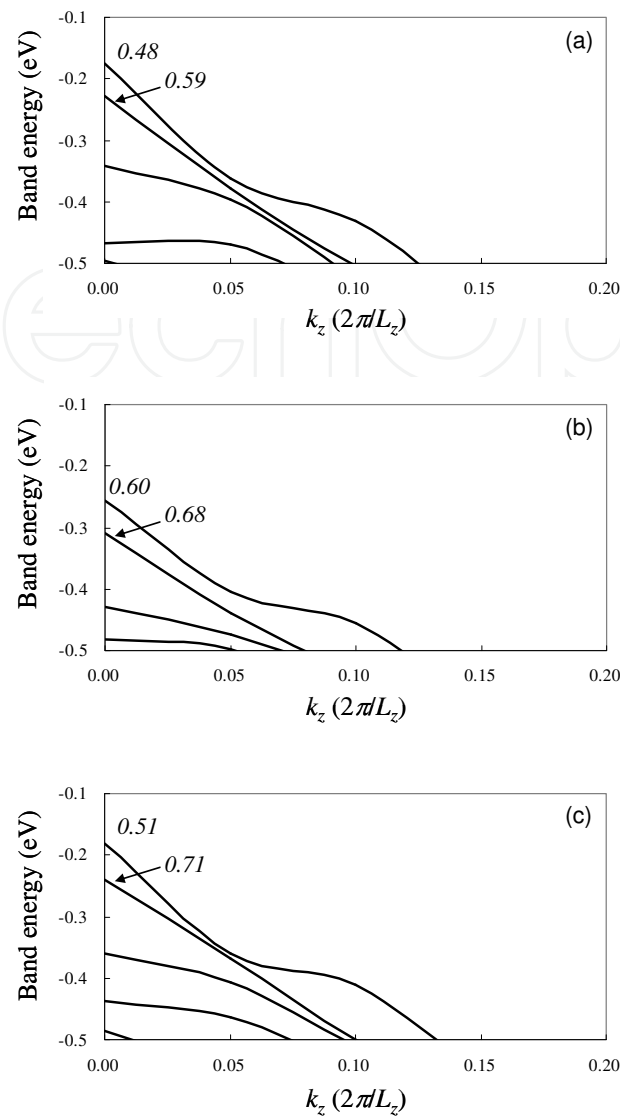The effective mass is generally given by a 3×3 tensor. The reciprocal matrix of effective mass is defined as

Fig. 11. Band diagram of $Si_{80}H_{28}\langle 110 \rangle$ SiNW model in the vicinity of the valence-band top: (a)–(c) denote the same conditions as those in Fig. 8. Italic numbers denote the effective masses in units of m_0.

$$(m_j^*)^{-1} = \pm \frac{1}{\hbar^2} \begin{pmatrix} \dfrac{\partial^2 E_j}{\partial k_x^2} & \dfrac{\partial^2 E_j}{\partial k_x \partial k_y} & \dfrac{\partial^2 E_j}{\partial k_x \partial k_z} \\[2mm] \dfrac{\partial^2 E_j}{\partial k_y \partial k_x} & \dfrac{\partial^2 E_j}{\partial k_y^2} & \dfrac{\partial^2 E_j}{\partial k_y \partial k_z} \\[2mm] \dfrac{\partial^2 E_j}{\partial k_z \partial k_x} & \dfrac{\partial^2 E_j}{\partial k_z \partial k_y} & \dfrac{\partial^2 E_j}{\partial k_z^2} \end{pmatrix}, \qquad (7)$$

where $\hbar$ is equal to Planck's constant divided by 2π. On the right hand, a positive sign is adopted for carrier electrons and a negative sign for holes. As mentioned above, the band energies of our SiNW models remain constant along the transverse directions, namely,
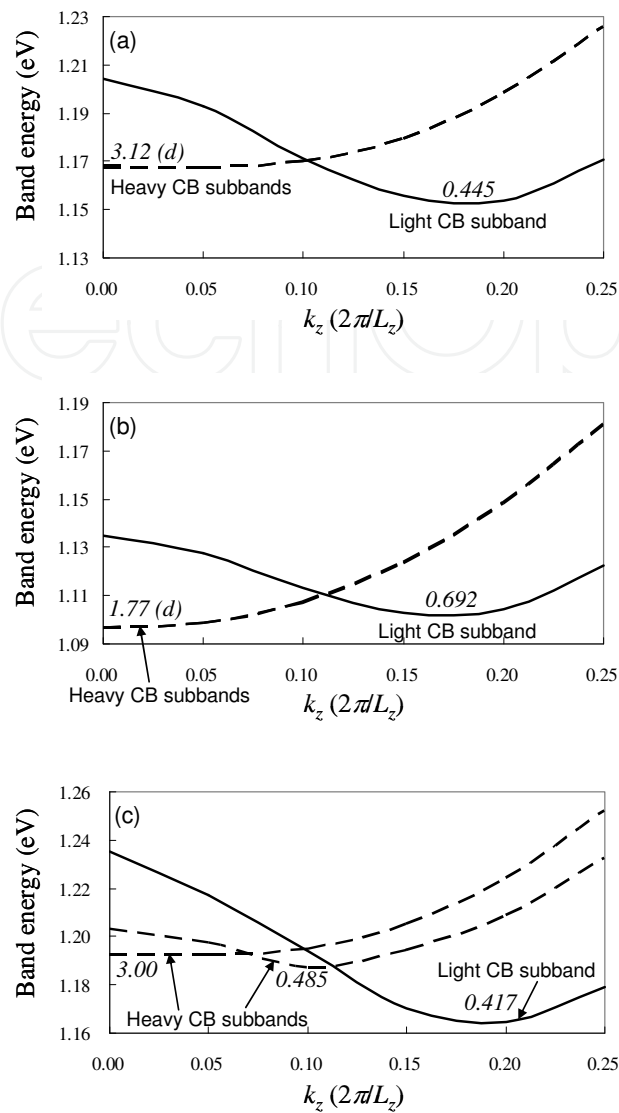
Fig. 12. Band diagram of Si$_{74}$H$_{42}$⟨111⟩ SiNW model in the vicinity of the conduction-band bottom: (a)–(c) denote the same conditions as those in Fig. 8. Italic numbers denote the effective masses in units of m_0. *(d)* indicates degenerate subbands.

$$\partial E_j / \partial k_x = \partial E_j / \partial k_y = 0, \tag{8}$$

and therefore, the effective mass of the *j*th band for the SiNW models can be defined simply as a scalar,

$$m_j{}^* = \pm \hbar^2 \left(\partial^2 E_j \big/ \partial k_z^2 \right)^{-1} \tag{9}$$

at the maximum or minimum of E_j. The second derivative on the right hand of eq. (9) has been estimated numerically as

$$\frac{\partial^2 E_j[k_z]}{\partial k_z^2} = \frac{E_j[k_z + \Delta k_z] + E_j[k_z - \Delta k_z] - 2E_j[k_z]}{(\Delta k_z)^2} \tag{10}$$
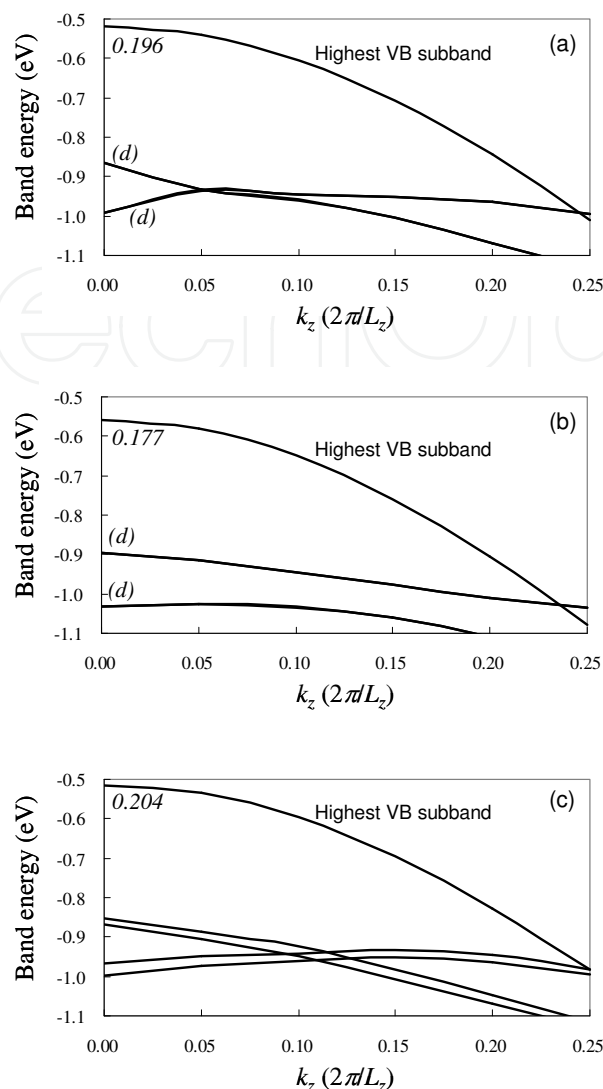
Fig. 13. Band diagram of $Si_{74}H_{42}\langle 111\rangle$ SiNW model in the vicinity of the valence-band top: (a)–(c) denote the same conditions as those in Fig. 8. Italic numbers denote the effective masses in units of m_0. (d) indicates degenerate subbands.

with $\Delta k_z = 0.05 \times (2\pi L_z)$. For the relaxation time, we have introduced the approximation that all of the band relaxation times are equal and constant regardless of stress. This procedure seems to be rough to some extent, but the variation rate of carrier conductivity can be easily and adequately represented in consideration of the canceling of almost part of band relaxation times (Nakamura et al., 2009b).

5. Prediction of piezoresistance coefficients

The longitudinal piezoresistance coefficient π_l and the transverse one π_t are given by

$$\pi_l = \Delta\rho_l / \rho_0\sigma_l; \ \pi_t = \Delta\rho_t / \rho_0\sigma_t, \tag{11}$$

where $\sigma_{l,t}$ are the longitudinal and transverse tensile stresses, ρ_0 is the resistivity along the wire axis without stress, and $\Delta\rho_{l,t}$ are variations in ρ_0 due to $\sigma_{l,t}$. On the approximation of

band relaxation times mentioned above, eq. (11) in the n- and p-type states is rewritten with respect to strain ε as follows,

$$(\pi_\alpha)^n = \frac{1}{Y_\alpha \varepsilon_\alpha} \left(\sum_{j \in CB} \frac{n'_{j,0}}{n'_{j,\alpha}} \frac{m_{e,j,\alpha}^*}{m_{e,j,0}^*} - 1 \right);$$ (12)

$$(\pi_\alpha)^p = \frac{1}{Y_\alpha \varepsilon_\alpha} \left(\sum_{j \in VB} \frac{p'_{j,0}}{p'_{j,\alpha}} \frac{m_{h,j,\alpha}^*}{m_{h,j,0}^*} - 1 \right),$$ (13)

where n'_j and p'_j are defined in eqs. (5) and (6), respectively, and Y is Young's modulus leading to normal stress with a linear response approximation according to the classical Hooke's law,

$$\sigma_l = Y_l \varepsilon_l; \quad \sigma_t = Y_t \varepsilon_t,$$ (14)

Subscript α in eqs. (12) and (13) denotes l or t, which means a property in relation to longitudinal or transverse tensile strain, and 0 denotes the strain-free condition. The value of ε_α is 0.01 strain for all cases in this chapter, and we assumed Y_α to be the experimental values of Young's modulus of bulk silicon (Wortman & Evans, 1965); 130.2 GPa for longitudinal and transverse tensile stresses in the $Si_{89}H_{44}\langle 001 \rangle$ model, 168.9 GPa for both tensile stresses in the $Si_{80}H_{28}\langle 110 \rangle$ model, and 187.5 GPa for longitudinal tensile stress and 168.9 GPa for transverse one in the $Si_{74}H_{42}\langle 111 \rangle$ model.

Table 2 summarizes calculation results of the piezoresistance coefficients with respect to δ. Obviously, the values of $(\pi_{l\langle 001 \rangle})^p$, longitudinal piezoresistance coefficients for the p-type $Si_{89}H_{44}\langle 001 \rangle$ model, are by far the largest in Table 2. We have obtained 147×10^{-11} Pa^{-1} for $(\pi_{l\langle 001 \rangle})^p$ with δ = 10^{-4} (Nakamura et al., 2008), and it is expected that p-type $\langle 001 \rangle$ SiNW will have giant longitudinal piezoresistivity, in consideration of the result that $(\pi_{l\langle 001 \rangle})^p$ is about 10 times as large as $(\pi_{l\langle 110 \rangle})^p$, which has been measured experimentally as 38.7×10^{-11} Pa^{-1} (Toriyama & Sugiyama, 2003), with a small carrier density.

δ	Carrier (cm^{-3})	n-doped piezoresistance constant (10^{-11} Pa^{-1})					
		$\pi_{l\langle 001 \rangle}$	$\pi_{t\langle 001 \rangle}$	$\pi_{l\langle 110 \rangle}$	$\pi_{l\langle 110 \rangle}$	$\pi_{l\langle 111 \rangle}$	$\pi_{t\langle 111 \rangle}$
10^{-4}	5×10^{16}	−3.37	0.84	−1.02	12.1	19.6	−19.2
10^{-3}	5×10^{17}	−3.66	0.63	−1.00	12.1	19.6	−19.1
10^{-2}	5×10^{18}	−3.66	0.77	−1.18	12.1	19.5	−18.8
δ	Carrier (cm^{-3})	p-doped piezoresistance constant (10^{-11} Pa^{-1})					
		$\pi_{l\langle 001 \rangle}$	$\pi_{t\langle 001 \rangle}$	$\pi_{l\langle 110 \rangle}$	$\pi_{l\langle 110 \rangle}$	$\pi_{l\langle 111 \rangle}$	$\pi_{t\langle 111 \rangle}$
10^{-4}	5×10^{16}	147	−1.44	14.2	4.71	−4.87	2.60
10^{-3}	5×10^{17}	146	−1.41	14.4	4.72	−4.87	2.60
10^{-2}	5×10^{18}	146	−1.41	14.1	4.53	−4.87	2.60

Table 2. Theoretical values of piezoresistance coefficients for H-terminated SiNW models

A sign of the giant longitudinal piezoresistivity in p-type H-terminated $\langle 001 \rangle$ SiNW can be observed in the variations of the VB structure. The $Si_{89}H_{44}\langle 001 \rangle$ model has four VB subbands in the vicinity of the VB top as shown in Fig. 9. The highest VB subband of those without

stress [Fig. 9(a)] has a small hole effective mass, called *the light-hole subband*, and by contrast, two of the second highest VB subbands in degeneracy have a larger hole effective mass, called *the heavy-hole subbands*. The uniaxial tensile stress in the [001] longitudinal direction [Fig. 9(b)] causes a sharp drop in the band energy of the light-hole subband, leading to the alternation of the order of band energy levels between the light-hole subband and the heavy-hole subbands, and then most of the holes will be redistributed to the heavy-hole subbands where hole effective mass is markedly raised due to the longitudinal tensile stress. This sudden change in the hole occupation with the increase in effective mass will bring a significant decrease in the hole conductivity in the p-type H-terminated ⟨001⟩ SiNW. The hole occupation numbers and effective masses of each band with/without stress are summarized in Table 3. $(\pi_{t\langle001\rangle})^p$ should be very small because the hole occupation numbers and effective masses do not change so much due to the transverse tensile stress. Similarly, a drastic change due to tensile stresses in the carrier distribution or effective masses is not seen in Figs. 8, 10, and 11.

	strain-free		1% longitudial tensile-strained		1%transverse tensile-strained	
Subband	$p_j V / \delta$	$m_{h,j}/m_0$	$p_j V / \delta$	$m_{h,j}/m_0$	$p_j V / \delta$	$m_{h,j}/m_0$
Light-hole	0.601	3.00	0.131	3.15	0.716	3.01
Heavy-hole	0.193	4.74	0.415	29.4	0.257	4.52
	0.193	4.74	0.415	29.4	0.023	4.76
4th highest	0.012	1.29	0.038	1.23	0.004	1.33

Table 3. Hole occupation numbers and effective masses of each band in the $Si_{89}H_{44}\langle001\rangle$ model for $\delta = 10^{-3}$; m_0 denotes the rest mass of an electron

For the $Si_{74}H_{42}\langle111\rangle$ model, the band energy of the highest VB subband shown in Fig. 13 is maximized at the Γ point. As seen in the band structure of the same model (Li & Freeman, 2006), the highest VB subband is located far from other lower subbands by more than 0.3 eV at the Γ point. Thus, it is easily found that most holes (more than 99.999% at 300 K) occupy the highest VB subband if there are no dangling bonds on the wire wall. The change in the hole occupation, as observed in the H-terminated ⟨001⟩ SiNW model, cannot take place, and accordingly, the conductivity depends only on the hole mobility or the band hole effective mass of the highest VB subband. Our calculation results of the band hole effective mass, 0.177–0.204, are not greatly affected by tensile strains, and as a result, no drastic change due to strain in the conductivity can be expected.

The longitudinal and transverse piezoresistance coefficients for the p-type H-terminated ⟨111⟩ SiNW model are very small and not dependent on temperature or hole concentration, because their values do not contain the contribution from the change in hole distribution controlled by temperature and concentration. The result that piezoresistance coefficients for p-type H-terminated ⟨111⟩ SiNW are small seems to be contradictory to the experimental result (He & Yang, 2006). However, in their experiment, SiNWs with a giant piezoresistancre coefficient could be obtained in a very low ratio. It is natural for SiNWs with a giant piezoresistance coefficient to be under an irregular wall-termination condition, not normal oxidation.

Contrary to the VB top, three subbands lie close together on the CB bottom, where the minima of their band energies are within a range less than 0.03 eV. In the band diagrams

without strain, shown in Fig. 12(a), we can observe band crossing between a nondegenerate subband minimized on the way along the reciprocal path with a small carrier effective mass, called *the light CB subband*, and a pair of doubly degenerate bands minimized at the Γ point with large carrier effective masses, called *the heavy CB subbands*. As shown in Fig. 12(b), the degeneracy in the heavy CB subbands is not lifted by the longitudinal stress because the threefold rotational symmetry of the SiNW model is maintained. The longitudinal tensile stress can control which of the minima of band energies will be the lowest, leading to the redistribution of carrier electrons from the light CB subband to the heavy CB subbands with increasing effective mass. Therefore, it is expected that the conductivity of n-type ⟨111⟩ SiNW will be reduced under longitudinal uniaxial tensile stress.

On the other hand, the degeneracy in the heavy CB subbands should be lifted by transverse stress, and we found that one of the heavy CB subbands give rise to a new minimum of band energy with small effective mass, as shown in Fig. 12(c). This change in the effective mass for the heavy CB subband owing to the transverse uniaxial tensile stress will cause a significant increase in the carrier electron conductivity. Although a meaningful change in the carrier-electron conductivity owing to stresses can be observed in n-type H-terminated ⟨111⟩ SiNW, $(\pi_{l\langle 111 \rangle})^n$ and $(\pi_{t\langle 111 \rangle})^n$ are also much smaller than $(\pi_{l\langle 001 \rangle})^p$. We can conclude that ⟨111⟩ SiNW, particularly in the p-type semiconductor state, is not a suitable candidate for nanoscale piezoresistors.

6. Conclusions

We have simulated the piezoresistance coefficients in H-terminated single-crystal SiNWs on the basis of first-principles calculations of model structures. The carrier conductivity along the wire axis has been calculated using band carrier densities and their corresponding effective masses derived from the one-dimensional band diagram by a novel approach for a small amount of carrier occupation. In the $Si_{89}H_{44}$⟨001⟩ SiNW model, the uniaxial tensile stress in the longitudinal direction causes a sharp drop in the band energy of the highest VB subband, called the light-hole subband, leading to the redistribution of holes to the VB subbands with a huge hole effective mass, called the heavy-hole subbands. The sudden change in the hole occupation with the increase in effective mass will bring a drastic decrease in the hole conductivity, and as a result, we have obtained a giant piezoresistance coefficient of 147×10^{-11} Pa^{-1} for the longitudinal piezoresistance coefficient for p-type H-terminated ⟨001⟩ SiNW with a small carrier density. It is well known that the bulk p-type ⟨001⟩ silicon is not useful for the piezoresistor due to its very low piezoresistive coefficient (Smith, 1954). However, it is found that p-type H-terminated ⟨001⟩ SiNW will be one of the most suitable candidates for nanoscale piezoresistors due to its giant piezoresistivity.

For p-type ⟨111⟩ SiNW, most holes occupy the highest VB subband if there are no dangling bonds on the wire wall, and therefore, the longitudinal and transverse piezoresistance coefficients for p-type H-terminated ⟨111⟩ SiNW are very small, in contrast to those in the case of p-type bare-walled ⟨111⟩ SiNW with dangling bonds (Cao et al., 2007). For n-type ⟨111⟩ SiNW, the longitudinal and transverse piezoresistance coefficients are also much smaller than the longitudinal one for the p-type ⟨001⟩ SiNW model. We predict that ⟨111⟩-oriented SiNW will not be a suitable candidate for nanoscale piezoresistors.

7. References

Bockstedte, M.; Kley, A.; Neugebauer, J. & Scheffler, M. (1997). Density-functional theory calculations for poly-atomic systems: electronic structure, static and elastic properties and ab initio molecular dynamics. *Computer Physics Communication,* Vol. 107, No. 1-3, 187-222, ISSN 0010-4655

Bui, T. T.; Dao, D. V.; Nakamura, K.; Toriyama T. & Sugiyama, S. (2009). Evaluation of the piezoresistive effect and temperature coefficient of resistance in single crystalline silicon nanowires, *Proceedings of 2009 International Symposium on Micro-Nano Mechatronics and Human Science*, pp. 462-466, ISBN 978-1-4244-5095-4, Nagoya, Japan, November 2009, IEEE

Cao, J. X.; Gong, X. G. & Wu R. Q. (2007). Giant piezoresistance and its origin in Si(111) nanowires: first-principles calculations. *Physical Review B,* Vol. 75, No. 23, 233302 (4 pages), ISSN 1098-0121

Hamann, D. R. (1989). Generalized norm-conserving pseudopotentials. *Physical Review B,* Vol. 40, No. 5, 2980-2987, ISSN 1098-0121

He, R. R. & Yang, P. D. (2006). Giant piezoresistance effect in silicon nanowires. *Nature Nanotechnology,* Vol. 1, No. 1, 42-46, ISSN 1748-3387

Hohenberg, P. & Kohn, W. (1964). Inhomogeneous electron gas. *Physical Review,* Vol. 136, No. 3B, B864-B871, ISSN 0031-899X

Kittel, C. (2005). *Introduction to Solid State Physics, 8th edition,* Wiley, ISBN 978-0-471-41526-8, New York

Kresse, G. & Hafner, J. (1993). Ab initio molecular dynamics for liquid metals. *Physical Review B,* Vol. 47, No. 1, 558-561, ISSN 1098-0121

Kresse, G. & Furthmüller, J. (1996). Efficient iterative schemes for ab initio total-energy calculations using a plane-wave basis set. *Physical Review B,* Vol. 54, No. 16, 11169-11186, ISSN 1098-0121

Li, J. & Freeman, A. J. (2006). First-principles determination of the electronic structures and optical properties of one-nanometer (001) and (111) Si nanowires. *Physical Review B,* Vol. 74, No. 7, 075333 (7 pages), ISSN 1098-0121

Nakamura, K.; Isono, Y. & Toriyama T. (2008). First-principles study on piezoresistance effect in silicon nanowires. *Japanese Journal of Applied Physics,* Vol. 47, No. 6, 5132-5138, ISSN 0021-4922

Nakamura, K.; Isono, Y.; Toriyama T. & Sugiyama S. (2009a). First-principles simulation on orientation dependence of piezoresistance properties in silicon nanowires. *Japanese Journal of Applied Physics,* Vol. 48, No. 6, 06FG09 (5 pages), ISSN 0021-4922

Nakamura, K.; Isono, Y.; Toriyama T. & Sugiyama S. (2009b). Simulation of piezoresistivity in n-type single-crystal silicon on the basis of first-principle band structure. *Physical Review B,* Vol. 80, No. 4, 045205 (11 pages), ISSN 1098-0121

Perdew, J. P.; Burke, K. & Ernzerhof, M. (1996). Generalized gradient approximation made simple. *Physical Review Letters,* Vol. 77, No. 18, 3865-3868, ISSN 0031-9007

Sasaski, S.; Seki, T.; Imanaka K.; Kimata M.; Toriyama T.; Miyano, T. & Sugiyama, S. (2007). Batteryless-wireless MEMS sensor system with a 3D loop antenna, *Proceedings of the 6th Annual IEEE Conference on Sensors*, pp. 454-457, ISBN 978-1-4244-1262-5, Atlanta, USA, October 2007, IEEE, Los Alamitos

Smith, C. S. (1954). Piezoresistance effect in germanium and silicon. *Physical Review,* Vol. 94, No. 1, 42-49, ISSN 0031-899X

Toriyama T. & Sugiyama, S. (2003). Single crystal silicon piezoresistive nano-wire bridge. *Sensors and Actuators A,* Vol. 108, No. 1-3, 244-249, ISSN 0924-4247

Tufte O. N. & Stelzer, E. L. (1963). Piezoresistive properties of silicon diffused layers. *Journal of Applied Physics,* Vol. 34, No. 2, 313-318, ISSN 0021-8979

Wortman, J. J. & Evans R. A. (1965). Young's modulus, shear modulus, and Poisson's ratio in silicon and germanium. *Journal of Applied Physics,* Vol. 36, No. 1, 153-156, ISSN 0021-8979

Nanowires

Edited by Paola Prete

ISBN 978-953-7619-79-4

Hard cover, 414 pages

Publisher InTech

Published online 01, February, 2010

Published in print edition February, 2010

This volume is intended to orient the reader in the fast developing field of semiconductor nanowires, by providing a series of self-contained monographs focusing on various nanowire-related topics. Each monograph serves as a short review of previous results in the literature and description of methods used in the field, as well as a summary of the authors recent achievements on the subject. Each report provides a brief sketch of the historical background behind, the physical and/or chemical principles underlying a specific nanowire fabrication/characterization technique, or the experimental/theoretical methods used to study a given nanowire property or device. Despite the diverse topics covered, the volume does appear as a unit. The writing is generally clear and precise, and the numerous illustrations provide an easier understanding of the phenomena described. The volume contains 20 Chapters covering altogether many (although not all) semiconductors of technological interest, starting with the IV-IV group compounds (SiC and SiGe), carrying on with the binary and ternary compounds of the III-V (GaAs, AlGaAs, GaSb, InAs, GaP, InP, and GaN) and II-VI (HgTe, HgCdTe) families, the metal oxides (CuO, ZnO, ZnCoO, tungsten oxide, and PbTiO3), and finishing with Bi (a semimetal).

How to reference

In order to correctly reference this scholarly work, feel free to copy and paste the following:

Koichi Nakamura, Dzung Viet Dao, Yoshitada Isono, Toshiyuki Toriyama and Susumu Sugiyama (2010). Electronic States and Piezoresistivity in Silicon Nanowires, Nanowires, Paola Prete (Ed.), ISBN: 978-953-7619-79-4, InTech, Available from: http://www.intechopen.com/books/nanowires/electronic-states-and-piezoresistivity-in-silicon-nanowires

INTECH
open science | open minds